Research Article Vol. 38, No. 2 / February 2021 / Journal of the Optical Society of America A 237

Journal of the Optical Society of America A

OPTICS, IMAGE SCIENCE, AND VISION

3D printed millimeter-wave beam-steering reflector using dielectric fluids

MIGUEL RUPHUY[1,2,*] AND CARLOS E. SAAVEDRA[3,4]

[1]Queen's University, Kingston, Ontario K7L 3N6, Canada
[2]University of Costa Rica, San Pedro, 11501-2060 UCR, Costa Rica
[3]Department of Electrical and Computer Engineering, Queen's University, Kingston, Ontario K7L 3N6, Canada
[4]e-mail: saavedra@queensu.ca
*Corresponding author: miguel.ruphuychan@ucr.ac.cr

Received 21 October 2020; revised 21 December 2020; accepted 22 December 2020; posted 22 December 2020 (Doc. ID 413055); published 22 January 2021

A three-dimensional printed beam-steering reflector surface with dielectric fluids as the tuning agent is presented. The reflector is made using ECO-ABS with six rows of 19 parallel channels of square cross-sections. The permittivity of the ECO-ABS was measured at 2.55 with a loss tangent of 0.053. A conductor is placed at the back of the dielectric. The squared channels are filled with either distilled water or air. The effective permittivity within the reflector changes according to the material used to fill the channels. As an incident wave propagates through the printed dielectric, the configuration of air–water channels shapes the exiting phase front of the wave by locally controlling its phase delay. The resulting phase profile created by the air–water configuration leads to a steered beam. Numerical full-wave simulations show steerable angles ranging from −42° to 23° for a set of air–water configurations at 30 GHz. A prototype was fabricated and tested for the same configurations. Experiments confirm a wide range of angles starting at −40° up to 20°.

https://doi.org/10.1364/JOSAA.413055

1. INTRODUCTION

Millimeter-wave fifth-generation (5G) wireless networks are expected to transform how people and objects interact with the world around them. To overcome the issue of line-of-sight (LoS) obstructions in millimeter-wave links, femtocells and picocells will provide wireless coverage spanning tens of meters to hundreds of meters, respectively. In addition, because of LoS propagation issues, beam-steering is critical to the functioning of FPCs to deliver data to moving objects. The most common form of beam-steering is to use antenna arrays with time-delay circuitry at each antenna element. There are, however, other solutions that include reflecting surfaces that reflect and steer a beam at a desired arbitrary angle, which can potentially be used in conjunction with or even instead of standard antenna arrays.

Recently, Liu *et al*. [1] proposed a metasurface to steer a beam. Refraction is achieved by controlling the spacing between elements. Hence, there is a gradient of phase shifts from element to element. The resonant inclusions result in losses and a narrow bandwidth. A similar approach was taken by [2] where two metasurfaces were used. One metasurface concentrated the power as a lens and the other steered the beam. In the first case, the phase shift introduced by the metasurface was designed as a radial graded phase arrangement of cells. In the second case, the phase was linearly graded to refract the rays in the desired direction. Different angles are achieved by moving the antenna through the parallel arrangement of metasurfaces. The structure has high gain, although the footprint of the overall structure is large.

Several works have reported on the use of liquid crystals (LCs) for phase-shifting [3–5]. In [3], for instance, a tunable phase delay over electrically long transmission lines (∼5λ) connected to patch antennas is described. The tuned phase delay was achieved by biasing the liquid crystals to change its effective permittivity, but the feeding lines are impractically long. Another LC design involves metasurfaces to steer the beam. A metasurface was designed in [4] and placed on top of a guided-wave structure. The periodicity of the metasurface corresponds to the scan angle desired, while the LC tuning shifts the resonance frequency of the metasurface. Hence, the beam redirects as desired. The bandwidth is limited by the tunability of the elements instead of the resonance of the metasurface and the losses might be significant. Another method involving active frequency selective surfaces (AFSS) was proposed in [6]. A monopole was enclosed by FSS unit cells controlled with PIN diodes. The unit cells are configured to be transparent over a narrow band in the desired direction of propagation and reflective in the opposite direction.

Another method to steer a beam is by using high-impedance surfaces. Sievenpiper *et al*. [7] showed that a leaky wave antenna on top of a high-impedance surface and a printed board tuning layer made of periodic conductor squares can redirect a wave.

The steering occurs when the resonance frequency is ajusted by changing the capacitance of the unit cells, which results from laterally moving the adjustable layer. Small movements can have a large effect in the direction of propagation.

In recent years, solid dielectrics have been the subject of studies exploring beam steering. In [8], a multiwaveguide slot array is beam steered by moving a dielectric bar within the waveguide. The dielectric adds a constant phase shift between the slots, which results in constructive interference of the outgoing waves at different directions. The steering angle is approximately 10°. Ferroelectric materials with tunable permittivity such as barium strontium titanate and other materials such as lead niobate pyrochlores have been used to design reflectarrays. In [9], for example, a pyrochlore was used with a dual-band circularly polarized reflectarray to steer the reflected beam angle by 50° by tuning the permittivity of the material.

In the search for a steerable beam reflector that can handle large amounts of signal power over broad bandwidths, high-density plasmas have been investigated [10]. Notwithstanding the challenge in producing the plasma, this technique is intriguing in that it can be conformed to different geometries by modifying the external magnetic field that confines it.

An approach closer to the classical electronically controlled technologies was proposed in [11], where multiple antennas are placed behind a hemi-ellipsoidal lens at different locations and a switch selects one antenna to transmit. The antenna's position with respect to the axis of the lens determines the propagation direction of the outgoing wave.

In this paper, a three-dimensional (3D) printed reflecting surface in which the beam-steering is executed using dielectric fluids is presented. Beam-steering reflecting surfaces can be located inside buildings, for example, to direct millimeter-wave signals around hallway corners or through doorways, thereby potentially reducing the number of femtocells needed to cover a certain area. While microfluidic techniques have been previously reported at high frequencies for focal plane arrays [12], phase shifters [13,14], reconfigurable antennas [15], tunable couplers [16], and other components [17], to the best of our knowledge, this work is the first known reflector that simultaneously uses additive manufacturing and microfluidics to yield an effective, tunable, low-cost beam-steering structure at millimeter-wave frequencies. As presented earlier in the introduction, most work on beam-steering has focused on electronic steering, loading antennas with solid dielectrics or conductors.

2. CONCEPT

In [18], an electrically thin reflector based on phase profiling was designed. The reflector is shined by a perpendicularly incident plane wave. The phase profile is achieved by stacking slabs of dielectric materials, as shown in Fig. 1, and selecting the dielectric constant in the material such that the incoming wave exits the reflector with an angle. The wave traverse the dielectrics two times: once when it is incident and once when it is reflected back. The phase of the perpendicularly incident wave is the same all over the surface as it enters the reflector. Assuming no coupling between dielectrics, the waves can be considered to be confined within each material. The wave at each material moves at different phase velocities, with a phase shift that corresponds

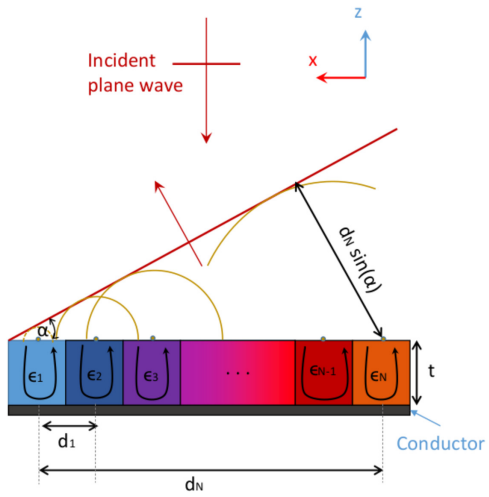

Fig. 1. Electrically thin reflector.

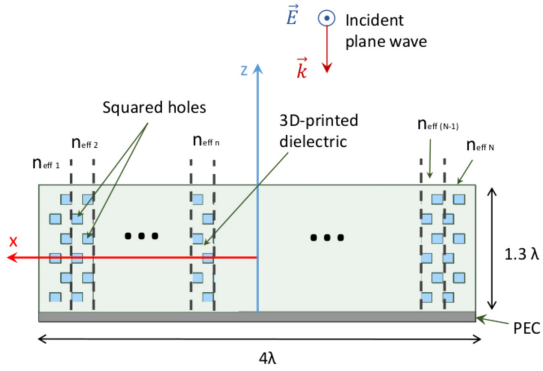

Fig. 2. View of the fluidically tunable reflector along the xz plane. The length λ is 10 mm, corresponding to the free-space wavelength of a 30 GHz signal.

to $2k_0\sqrt{\epsilon_n}t$, where k_0 is the wavenumber, ϵ_n is the permittivity of the nth material, and t is the thickness of the dielectrics. If the outgoing wave is represented as a set of Huygens' principle sources, a phase front forms from the constructive interference of the different Huygens' sources, as can be appreciated in Fig. 1. In such a design, the assumption of minimal coupling between materials is valid as long as t is much smaller than the wavelength.

A design equation can be derived by equating the phase path of the wave of different ray paths [18]. Starting at the surface of the reflector, going through the dielectrics and back out until the wave reaches the desired phase front (red line with an angle α in Fig. 1). All rays have to conform to this phase path to have a constructive interference in the outgoing wave. This path can be captured by

$$2tk_0n_1 = 2tk_0n_n + d_n \sin(\alpha)k_0, \tag{1}$$

where n_n is the refractive index of the nth layer, d_n is the distance from the leftmost layer of the reflector to the nth layer, and α is the steered angle.

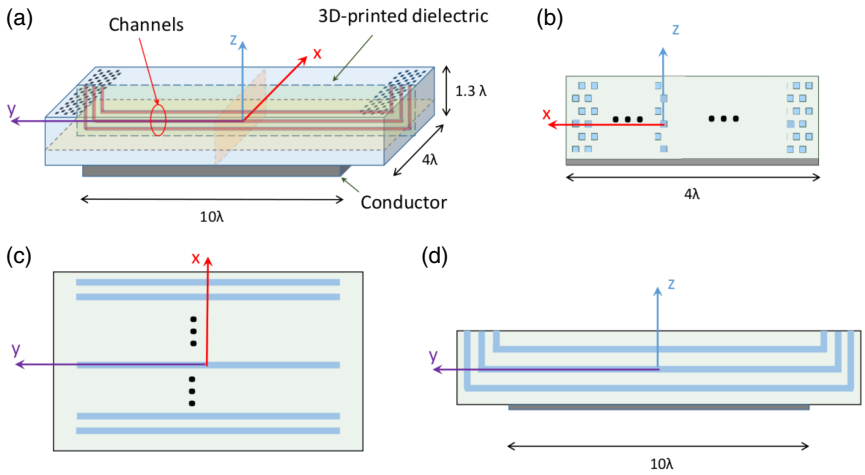

Fig. 3. Tunable reflector design: (a) 3D schematic of the reflector; (b) xz cut of the reflector; (c) xy cut of the reflector; and (d) yz cut of the reflector.

3. DESIGN

Following the concept discussed in the previous section of phase tuning the wave, a similar but tunable design is proposed here. To have an steerable reflector, a 3D printed device is designed with a set of squared channels with a dimension of 1 mm per side and a conductor on the bottom, as shown in Fig. 2. The 1 mm dimension corresponds to $\lambda/10$, where λ is the wavelength of a 30 GHz signal in free space. ECO-ABS is used as the dielectric printed material, which was characterized at 30 GHz using the rectangular waveguide method [19]. The obtained parameters are $\epsilon_r = 2.55$ with a loss tangent of 0.053. In the case of water, the permittivity was obtained from [20], where Banting *et al*. performed a frequency sweep measurement from 500 MHz to 40 GHz using the commercially available probe N1501A-10. The dielectric constant corresponds to 26.9 with a loss tangent of 1.25 at 30 GHz.

Additional features are added to the final printed model to facilitate filling the channels with dielectric fluids. A 3D configuration of the reflector is shown in Fig. 3(a), where only three of the channels were drawn for clarity. The cuts in every plane are shown in Figs. 3(b), 3(c), and 3(d). The added feature is best appreciated in Fig. 3(d), where U-shaped channels are used to take advantage of gravity when filling a selection of channels with the dielectric fluid. The electric conductor is placed on the bottom of the printed material and covers only the part of the channels that are parallel to the conductor. Figure 4 shows 3D exploded views of the same reflector. The structure has one horizontal and one vertical cut to improve the visualization of the channels within the ECO-ABS material. Additionally, four hangers are printed on the sides to easily attach the reflector to an absorber wall.

The squared channels can be filled with distilled water or be left with just air. To decide which channels should have air or water, the reflector is conceptually divided into sets of six squared channels for analysis, as shown in Fig. 2. The steered angle is achieved by filling a selection of channels, each angle having a different configuration. The number of channels that are filled with water determines the phase shift that a perpendicularly incident wave will have. Hence, the number of degrees of freedom is determined by the number of possible combinations. For example, all six channels could be filled with air, or there could be one channel filled with water and the remaining five filled with air, and so on, for all possible sets. Each of these combinations have an effective refractive index associated with it, and it is estimated by finding the weighted average of the refractive index of water, air, and ECO-ABS material over the area that they cover in a section. The effective refractive index values of all combinations found are shown in Table 1.

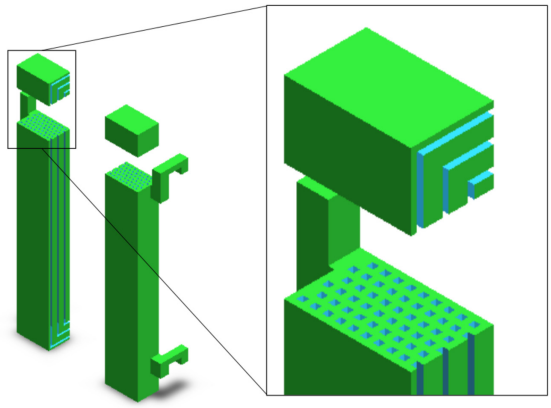

Fig. 4. Exploded views of the printed reflector.

Table 1. Effective Refractive Index Based on Channel Fillings

Number of Channels		
Air-Filled	Water-Filled	n_{eff}
6	0	1.46
5	1	1.76
4	2	2.07
3	3	2.38
2	4	2.69
1	5	2.99
0	6	3.3

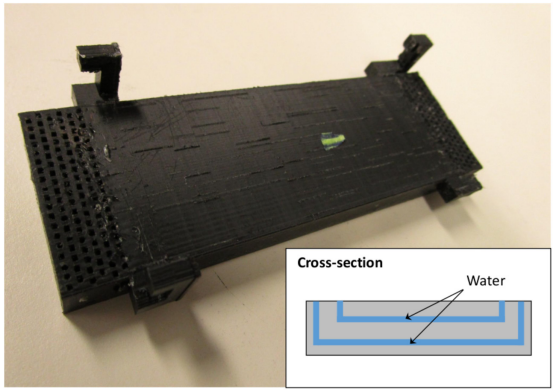

Fig. 5. Photograph of the 3D printed millimeter-wave reflector.

This calculated refractive index is used to estimate the phase shift that the wave experiences. However, this calculation only serves as a guide and not as an accurate prediction of the overall physics. Besides having a discrete design, there are other important factors to consider such as the reflector thickness. For a mechanically robust design, the reflector had to be electrically thick. This implies that the wave has to travel longer over an inhomogeneous material. Each channel is 1 mm wide ($\lambda/10$), and the ones filled with water show a high contrast when compared to its neighboring regions. This creates many diffraction patterns within the reflector that are not accounted for in Eq. (1), which is useful as a first approximation to calculate the initial reflector geometry. Final reflector dimension values are found through optimization using Ansys HFSS, a full-wave electromagnetic simulator.

4. RESULTS

A photograph of the 3D printed millimeter-wave reflector is shown in Fig. 5. A Dremel Digilab 3D printer was used to fabricate the reflector using a 1.75 mm diameter ECO-ABS filament. The printer is configured under the highest resolution (0.05 mm) and the reflector dimension in the y axis is set to 10λ, while the dimensions in x and z are 4λ and 1.3λ, respectively, as shown in Fig. 2. The permittivity of the filament material used for 3D printing was characterized in a WR-28 waveguide environment. An Anritsu VectorStar MS4644B vector network analyzer (VNA) was calibrated using the thru-reflect-line (TRL) method. A short length of WR-28 was machined for the line standard. Once the calibration is completed, a piece of printed ECO-ABS material is placed within the waveguide and the S-parameters are measured from which the permittivity was extracted using the method described in [19]. The permittivity of the ECO-ABS at 30 GHz was determined to be 2.55 with a loss tangent of 0.053.

The experiment is set on top of an optic table and all measurements reported here were taken at 30 GHz. Absorbers are positioned over the table and on two walls around the setup to minimize reflections. The reflector is fixed on one of these walls; whereas one of the horn antennas acts as the plane wave excitation of the numerical simulation. This horn antenna has a fixed position at a distance far from the reflector ($\approx 33\lambda$). The second antenna is moved along a semi-circle capturing data every 10 deg, as shown in Fig. 6. The horn antennas have an

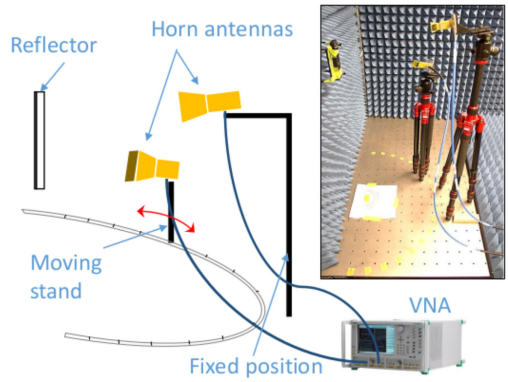

Fig. 6. Experiment setup.

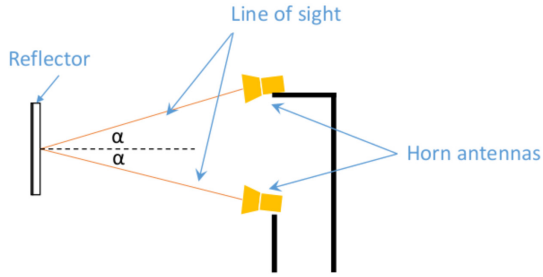

Fig. 7. Side view of the experiment setup.

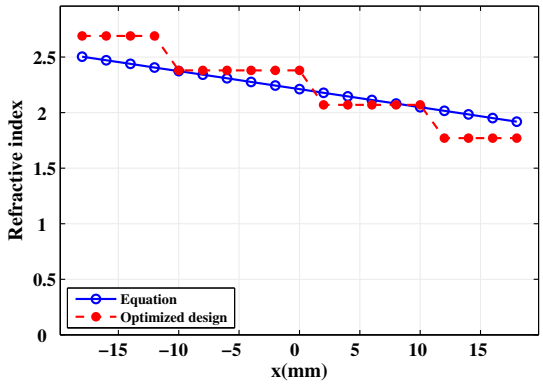

Fig. 8. Refractive index profile. In blue, the approximated design using Eq. (1). In red, the optimized numerically simulated design.

angle of $\alpha = 12°$ with respect to the horizontal axis, as shown in Fig. 7. The opening of the channels of the reflector filled with air are first covered with silicon glue. Then the other openings are filled with water using a syringe and also sealed with silicon.

In our case study, a reflector for a 23 deg steered beam is first designed using Eq. (1) and then optimized with numerical simulations. Figure 8 shows the design equation results in blue, which is a continuous linear function, while the discrete optimized design is the red line. The mean squared error between the refractive index calculated using Eq. (1) and the optimized design using HFSS is only 2.48%.

This reflector configuration was numerically simulated using HFSS and experimentally tested. In the case of the numerical simulation, the reflector is excited by a perpendicular plane wave, the ECO-ABS material is configured with the measured

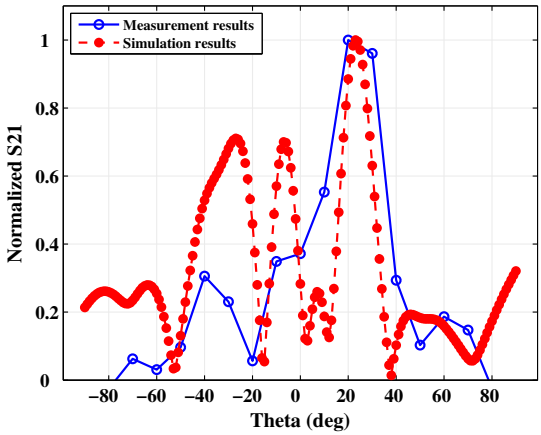

Fig. 9. S21 normalized parameter measurement in blue. Normalized farfield electric field intensity of the numerical simulation.

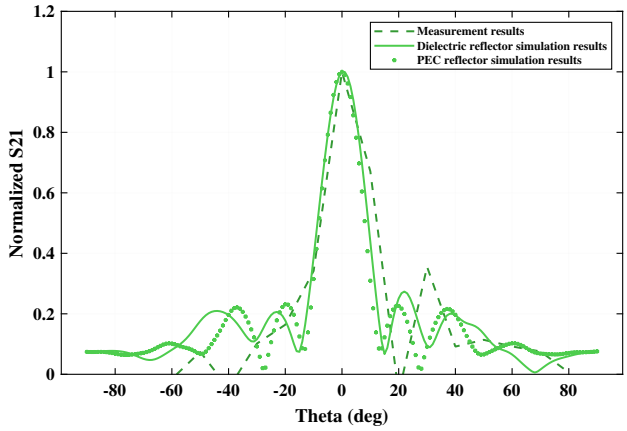

Fig. 10. Profile 1. Measured and simulated results of theta sweep for the steered angle of 0° in green solid line. Measurement results in dashed line. Simulation results of the PEC reflector is presented for comparison in dotted line.

permittivity values and at the back of the reflector a perfect electric conductor is placed. Periodic boundary conditions are used in the y axis to have an infinite reflector and reduce the computational time.

Two measurements are performed for this configuration. The first measurement goes through every position in the semi-circle with the reflector. A second measurement is taken with the same alignments and positioning of the antennas, but without the reflector. The second measurement is used to subtract the effect of coupling between the antennas. During the measurements, significant coupling was found when one antenna was in near proximity of the other one. Both antennas are aligned toward the reflector's position with a separation of approximately 13λ between them at the highest coupling. A clear non-negligible effect was found and considered.

Figure 9 shows the simulated results of the electric field intensity swept over θ and normalized for comparison in red. The measurement results of the S21 parameter also are normalized and the data is captured every 10 deg. Measurements correspond to the blue curve. The simulation results have the main lobe at 23 deg while the measurement results have the maximum at 20 deg. The secondary lobes are harder to capture given that the relative power received is lower than in the case of the main lobe. Noise and reflections have a higher impact on these lobes.

To estimate the power efficiency of the proposed reflector, the peak electric field intensity is found for a beam bounced from the structure and from a perfect electric conductor (PEC) minus the 3D printed material and water. The PEC surface is designed to have the same surface area as the proposed reflector. The peak electric field intensity of the reflected beam from the PEC is multiplied by the cosine of 23° to account for the effective area seen by the incident beam. The calculated efficiency of the proposed reflector from these two simulations is found to be 29%. The highest possible efficiency for the proposed reflector is expected when the 3D printed structure is filled only with air and the wave is incident perpendicular to the surface, corresponding to a 0° angle reflector. For this case, the efficiency is found to be 59.8%, using the methodology explained earlier. Figure 10 shows the normalized electric fields for a PEC reflector (dotted line) as well as for the dielectric fluid reflector with no water on the channels (solid line). Measurements are also included in the plot represented by the dashed line.

Another case is designed for having a maximum reflection at a −42° angle. In contrast to the first design, this case is optimized by running parametric simulations. At the beginning of the optimization, every channel is empty and only one is filled with water. Every channel position is tested as a water-filled channel until the highest electric field at the desired angle is achieved. The process is repeated, maintaining the configuration with the best desired outcome of the first iteration while the remaining empty channels are tested with distilled water filling one channel with water at a time. The process is iterated until the electric field at the designed angle no longer increases.

Figure 11 shows the refractive index profile of designs meant to steer the beam 0° and −42° in green and blue, respectively. The −42° reflector profile does not seem to follow any particular pattern. The reason for this may be that the channels are not necessarily filled from the bottom up (z direction) or from the top down (−z direction). Instead, the filled channels are scattered throughout the reflector and many wave scatterings happen within the dielectrics. These scatterings are the ones responsible for redirecting the ray. The efficiency for this case corresponds to 47.7%. Even though the efficiencies remain relatively low, there is a significant increase in the electric field in the desired direction compared to the case of having a PEC rectangle with the same footprint of the reflector being illuminated by a perpendicularly incident plane wave. The increase in the electric field is 258% and 188% for the 23° and −42° configurations, respectively.

The measured and simulated results for the −42° angle case is shown in Fig. 12. Similar to the first case, the main lobes are strong and the steering angle is closely predicted by simulation. In the case of the lower intensity lobes, possible causes for the discrepancy in the results are stray reflections in the test setup, as it was not fully enclosed by the absorber. However, the reflection at 0 deg is more evident in this case, even though the coupling between the antennas was considered. This systematic error leads us to study the imperfections of the 3D printed material.

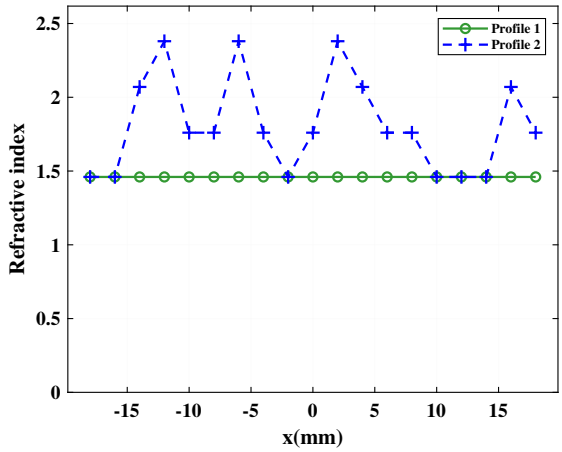

Fig. 11. Refractive index profile. Optimized numerically simulated design for the angles −42° and 0° in blue and green, respectively.

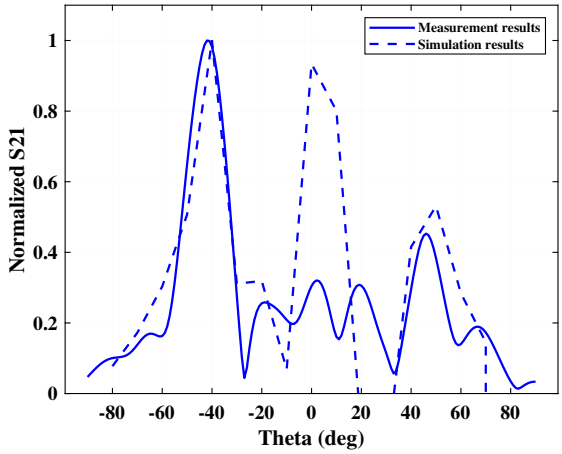

Fig. 12. Profile 2. Measured and simulated results of theta sweep for the optimized steered angle of −40° in blue solid line. Measurement results in dashed line.

The thickness of the reflector (thickness measure in the z direction) was found to be 0.2 mm higher than the designed value, increasing the reflection at 0°. According to the manufacturer, the resolution of the printer is 50 μm. The simulation results of the −42° angle reflector with side dimensions of the channels ±50 μm is shown in Fig. 13. In solid red, each channel is 50 μm smaller per side compared to the original design. In solid green, each channel is 50 μm larger per side than the original design. For comparison, the results are normalized and compared to the measurement results shown in dashed blue. By analyzing the results, it is clear that slightly larger channels agree better with the measurement results. In fact, if the channels are 70 μm larger than the original design per side, the simulation and measurement results show the highest similarity, as shown in Fig. 14. These results demonstrate that a high-quality, high-resolution printer is needed for best results, given the design's high degree of sensitivity to very small changes in the dimensions.

Using a 70 μm larger channel side dimension for comparison, the total change in volume can be calculated as $1.07\ \text{mm} \times 1.07\ \text{mm} \times 40\ \text{mm} = 45.8\ \text{mm}^3$ compared to the original design where the overall volume is given by

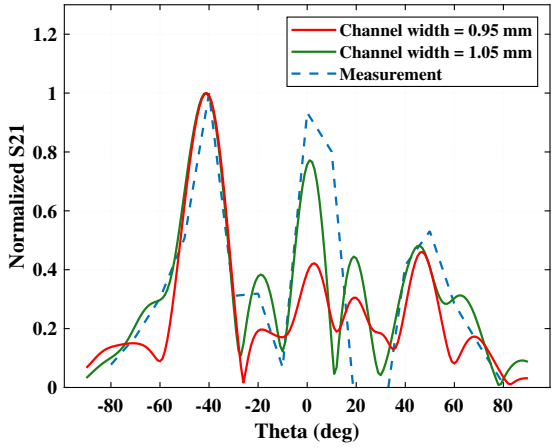

Fig. 13. Normalized electric field of the simulation for the −42° angle reflector. Channel width corresponds to 0.95 mm in red and 1.05 in green. Measurement is shown by the dashed blue line.

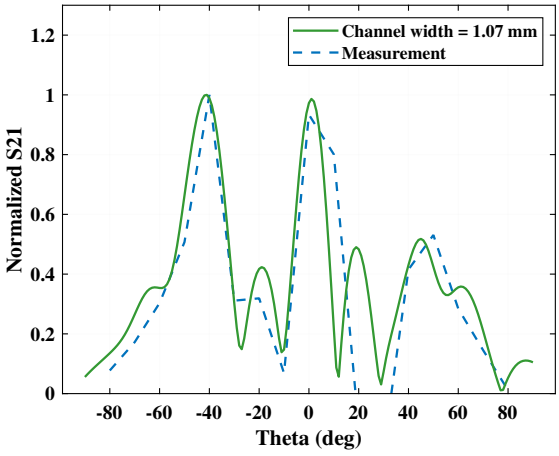

Fig. 14. Normalized electric field of the simulation for the −42° angle reflector. Channel width corresponds to 1.07 mm. Measurement is shown by the dashed blue line.

$1\ \text{mm} \times 1\ \text{mm} \times 40\ \text{mm} = 40\ \text{mm}^3$ per channel. The volume adds up to a significant amount to make a difference in the scattered field.

Furthermore, if the 2D problem is to be analyzed, the difference in area per channel is given by $(1.07\ \text{mm} \times 1.07\ \text{mm}) - 1\ \text{mm}^2 = 0.145\ \text{mm}^2$. This area must be multiplied by the number of channels filled with water to have a sense of the dimension of the extra area that has the highest refractive index contrast. There are 22 channels filled with water in the −42° reflector. Then, the total extra area of water in the reflector corresponds to $22 \times (0.145\ \text{mm}^2) = 3.19\ \text{mm}^2$, which is comparable and even greater than the area covered by a single channel ($1\ \text{mm}^2$). To estimate the switch time between configurations, let us consider the same case of −42°, where the total volume of the channels with the designed dimensions would be $(22 \times 40\ \text{mm}^3) = 880\ \text{mm}^3 = 0.88$ mL, with a commercially available pump (i.e., Reglo ICC Pump) it would take an estimate of 1.5 s at a flow rate of 0.58 mL/sec to fill the channels.

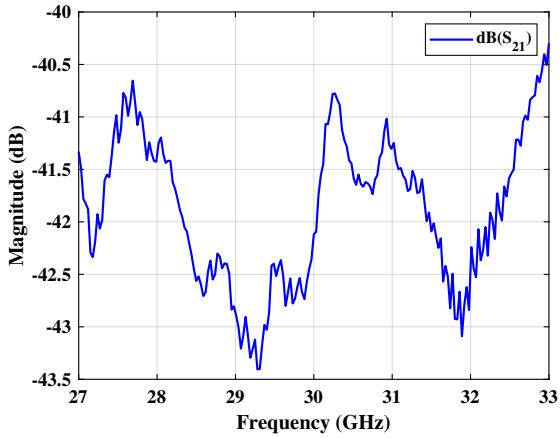

Fig. 15. Profile 2. Measured results of S21 at −40°.

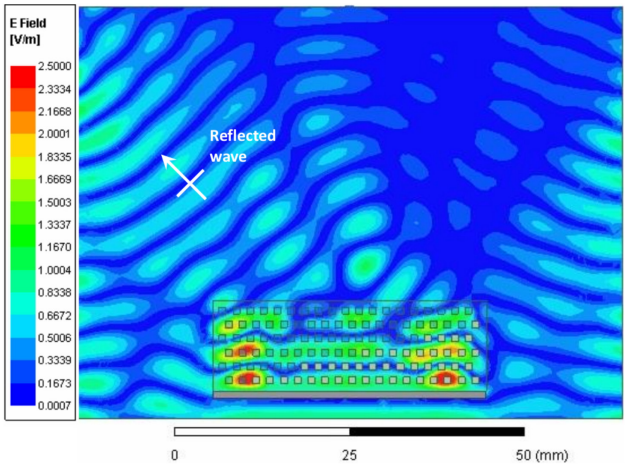

Fig. 16. Scattered electric field of the wave after traversing the reflector at 30 GHz.

Additionally, a frequency sweep from 27 GHz to 33 GHz of the measured S21 parameter at the designed angle was performed to study the frequency response. Figure 15 shows the frequency response of the reflector for an electric field peak at −40°. The −3 dB bandwidth covers the whole frequency sweep. Finally, Fig. 16 shows the scattered electric field intensity of the wave, demonstrating an outgoing wave with a flat phase front in the −42° angle.

Overall, the beam of the incident wave was effectively steered over a wide range of angles in the examples presented here. The flexibility of the reflector's design was demonstrated and the materials used were low cost and effective. The main disadvantage in the proposed solution here is the low efficiency. However, the electric field is increased for the designed angle effectively. Distilled water was used here for prototyping because it was convenient to find and easy to handle, but its freezing point restricts its use below 0°C. Yet, there are other dielectric fluids that can be used that have lower freezing points than pure water. For example, when water and ethanol (C_2H_6O) are mixed in a 4:10 ratio, the solution will have a freezing point of −37°C. When the ratio is 1:10, the freezing point drops to −73°C and so on. Other solutions with freezing points below 0°C are discussed in [20].

5. CONCLUSION

What we believe is a novel reflector design was proposed based on phase profiling the incident wave using microfluidics and air as the tuning agents. A reflector was designed and constructed using a 3D printer. The reflector consisted of multiple parallel channels distributed over an ECO-ABS dielectric case with an aluminum plate on its back. The reflector demonstrated its ability to steer a ray. The different examples provided here show tunable ranges between −42° and 23° on simulation and between −40° and 20° on experiments. Notice that the channels' pattern allows inversion of the tested configurations by inverting the pattern of the microwave liquid channels with respect to x, which can increase the tunable range. The reflector was build using a 3D printer, which is a cost-effective solution with dielectric materials. The measured main lobes are predicted with high accuracy. Further improvements to the original design can be achieved using materials with lower loss, either the printed dielectric or the microwave liquid. Also, the design can be thinner by decreasing the number and shape of the channels. Although this would limit the flexibility in terms of the angles that can be configured, it also would significantly decrease the losses. Finally, by modifying the flat surface to a concave shape the concentrating effect of the converging scattered wave would enhance the performance at the cost of a more complex design.

Funding. Natural Sciences and Engineering Research Council of Canada (RGPIN-2016-04784).

Disclosures. The authors declare no conflicts of interest.

REFERENCES

1. Y. Liu, X. Jin, X. Zhou, Y. Luo, K. Song, L. Huang, and X. Zhao, "A phased array antenna with a broadly steerable beam based on a low-loss metasurface lens," J. Phys. D **49**, 405304 (2016).
2. A. K. Singh, M. P. Abegaonkar, and S. K. Koul, "Wide angle beam steerable high gain flat top beam antenna using graded index metasurface lens," IEEE Trans. Antennas Propag. **67**, 6334–6343 (2019).
3. M. Nestoros, N. C. Papanicolaou, and A. C. Polycarpou, "Design of beam-steerable array for 5G applications using tunable liquid-crystal phase shifters," in *European Conference on Antennas and Propagation* (2019), pp. 1–4.
4. R. A. Stevenson, M. Sazegar, A. Bily, M. C. Johnson, and N. B. Kundtz, "Metamaterial surface antenna technology: commercialization through diffractive metamaterials and liquid crystal display manufacturing," in *International Congress on Advanced Electromagnetic Materials in Microwaves and Optics* (2016), pp. 349–351.
5. O. H. Karabey, A. Gaebler, S. Strunck, and R. Jakoby, "A 2-D electronically steered phased-array antenna with 2 x 2 elements in LC display technology," IEEE Trans. Microw. Theory Tech. **60**, 1297–1306 (2012).
6. L. Zhang, Q. Wu, and T. A. Denidni, "Electronically radiation pattern steerable antennas using active frequency selective surfaces," IEEE Trans. Antennas Propag. **61**, 6000–6007 (2013).
7. D. Sievenpiper, J. Schaffner, J. J. Lee, and S. Livingston, "A steerable leaky-wave antenna using a tunable impedance ground plane," IEEE Antennas Wirel. Propag. Lett. **1**, 179–182 (2002).
8. G. P. L. Sage, "Dielectric steering of a 3-D printed microwave slot array," IEEE Antennas Wirel. Propag. Lett. **17**, 2141–2144 (2018).
9. Q. Luo, S. Gao, Y. Wang, I. Bakaimi, A. Mostaed, C. K. de Groot, B. Hayden, and I. Reaney, "Electronically beam-steerable dual-band reflectarray for satellite communications," in *IEEE-APS Topical Conference on Antennas and Propagation in Wireless Communications* (2019), pp. 050–055.

10. J. Mathew, R. A. Meger, J. A. Gregor, R. E. Pechacek, R. F. Fernsler, and W. M. Manheimer, "Electronically steerable plasma mirror for radar applications," in *Proceedings International Radar Conference* (1995), pp. 742–747.
11. A. Artemenko, A. Mozharovskiy, A. Sevastyanov, V. Ssorin, and R. Maslennikov, "Electronically beam steerable lens antenna for 71–76/81–86 GHz backhaul applications," in *IEEE International Microwave Symposium* (2015), pp. 1–4.
12. A. Gheethan and G. Mumcu, "2D beam scanning focal plane array using microfluidic reconfiguration techniques," in *IEEE AP Symposium* (2014), pp. 1666–1667.
13. P. Meineri, D. Dubuc, and K. Grenier, "Liquid-based tunable loaded-line phase shifter," in *European Microwave Conference* (2012), pp. 719–722.
14. M. Brown, I. Goode, and C. E. Saavedra, "Lumped-element circuit modelling of microfluidic channels in microstrip transmission lines," in *IEEE NEWCAS Conference* (2018), pp. 31–34.
15. A. Singh, I. Goode, and C. E. Saavedra, "A multistate frequency reconfigurable monopole antenna using fluidic channels," IEEE Antennas Wireless Propag. Lett. **18**, 856–860 (2019).
16. M. Brown and C. E. Saavedra, "Tunable branchline coupler using microfluidic channels," IEEE Microw. Wireless. Compon. Lett. **29**, 207–209 (2019).
17. K. Entesari and A. P. Saghati, "Fluidics in microwave components," IEEE Microwave Mag. **17**, 50–75 (2016).
18. M. Ruphuy and O. M. Ramahi, "Refraction in electrically thin inhomogeneous media," J. Opt. Soc. Am. A **33**, 538–543 (2016).
19. V. V. Varadan and R. Ro, "Unique retrieval of complex permittivity and permeability of dispersive materials from reflection and transmitted fields by enforcing causality," IEEE Trans. Microw. Theory Tech. **55**, 2224–2230 (2007).
20. H. Banting and C. E. Saavedra, "Dielectric spectroscopy of fluids and polymers for microwave microfluidic circuits and antennas," IEEE Trans. Microw. Theory Tech. **69**, 337–343 (2021).